Comparison of fiber tracts derived from in-vivo DTI tractography with 3D histological neural tract tracer reconstruction on a macaque brain

Julien Dauguet,[a,*] Sharon Peled,[b] Vladimir Berezovskii,[c] Thierry Delzescaux,[d] Simon K. Warfield,[a] Richard Born,[c] and Carl-Fredrik Westin[e]

[a]Computational Radiology Laboratory, Children's Hospital, Brigham and Women's Hospital, Harvard Medical School, Boston, USA
[b]Harvard Center for Neurodegeneration and Repair, Boston, USA
[c]Department of Neurobiology, Harvard Medical School, Boston, USA
[d]Service Hospitalier Frédéric Joliot, CEA, Orsay, France
[e]Laboratory of Mathematics in Imaging, Brigham and Women's Hospital, Harvard, Medical School, Boston, USA

Since the introduction of diffusion weighted imaging (DWI) as a method for examining neural connectivity, its accuracy has not been formally evaluated. In this study, we directly compared connections that were visualized using injected neural tract tracers (WGA-HRP) with those obtained using in-vivo diffusion tensor imaging (DTI) tractography. First, we injected the tracer at multiple sites in the brain of a macaque monkey; second, we reconstructed the histological sections of the labeled fiber tracts in 3D; third, we segmented and registered the fibers (somatosensory and motor tracts) with the anatomical in-vivo MRI from the same animal; and last, we conducted fiber tracing along the same pathways on the DTI data using a classical diffusion tracing technique with the injection sites as seeds. To evaluate the performance of DTI fiber tracing, we compared the fibers derived from the DTI tractography with those segmented from the histology. We also studied the influence of the parameters controlling the tractography by comparing Dice superimposition coefficients between histology and DTI segmentations. While there was generally good visual agreement between the two methods, our quantitative comparisons reveal certain limitations of DTI tractography, particularly for regions at remote locations from seeds. We have thus demonstrated the importance of appropriate settings for realistic tractography results.
© 2007 Elsevier Inc. All rights reserved.

Keywords: Neural tracer; DTI tractography; Histology; 3D reconstruction

Introduction

Tracing neural connections lies at the heart of neuroanatomy and has profound implications for studying neural function as well as developmental and adult plasticity of the nervous system. It is also important for studying neurodegenerative diseases, and planning neurosurgical procedures, such as tumor ablation. Methods for tracing connections in the brain have a long history, beginning with those based on lesions and the resulting retrograde or antero-grade degeneration (Nissl in 1894, Marchi in 1886 and Nauta and Gygax in 1954). Subsequent methods have exploited the axonal transport of specific molecules, beginning with horseradish peroxidase (HRP) (La Vail and La Vail, 1972), which opened up a new era in neuroanatomy. This was followed by the discovery of a host of other tracers including small fluorescent molecules Bentivoglio et al. (1980); Kuypers and Ugolini (1990), lectins (Schwab et al., 1978), neurotrophins (Hendry et al., 1974), neurotoxins (Stoeckel et al., 1977), dextrans (Glover et al., 1986) and, more recently, carbo-cyanine dyes (Honig and Hume, 1986), latex microspheres (Katz et al., 1984) and viruses (Kuypers and Ugolini, 1990). While furnishing a powerful armamentarium with which to study connections in the brain, these methods, separately, and in combination, are highly invasive. Moreover, any histological visualization of the transported substance requires sacrifice of the experimental animal.

In the 1970s, water diffusion magnetic resonance imaging was introduced and later used for medical applications (LeBihan et al., 1986). With the introduction of diffusion tensor imaging (DTI), Basser et al. (1994) proposed representing the water diffusion coefficient distribution in all the directions of space as a tensor in each voxel. A reconstruction of the white matter pathways was later proposed based on this tensor model (Mori et al., 1999; Basser et al., 2000; Poupon et al., 2000; Westin et al., 2002). White matter tractography based on DTI became the first non-invasive, in-vivo technique for gross fiber tract tracing. Since then, many advanced methods and models have been proposed to improve the quality of the tractography (Tuch, 2004; Peled et al., 2006). The underlying assumption of diffusion-based tractography is that the water diffusion coefficient is

* Corresponding author. Fax: +1 617 582 6033.
 E-mail address: dauguet@bwh.harvard.edu (J. Dauguet).
 Available online on ScienceDirect (www.sciencedirect.com).

higher along the long axis of axons rather than perpendicular to it. Thus, the explicit quantity measured is water diffusion and not fibers. Moreover, since MRI methods typically calculate a macroscopic measure of a microscopic quantity (necessarily entailing intravoxel averaging), the voxel dimensions obtained influence the measured diffusion tensor at any given location in the brain.

As the sophistication of DTI tractography algorithms increases, it becomes essential to validate the results. These tractography techniques are already used in many neuroscience studies (see Mori and Zhang, 2006 for a review). It seems clear that DTI reveals gross connectivity as described in atlases based on histology (e.g. Nolte, 2002), but, as of yet, no rigorous validation of these techniques has been done. In particular, the performance of DTI tractography has not been established with respect to fiber decussations and the transition of fibers through a relay.

In evaluating DTI tractography, three main approaches have been proposed. The first is based on artificial ex-vivo data (phantoms) representing fibers and scanned using DTI (Lin et al., 2003; Perrin et al., 2005). A comparison between the known geometry expected and the DTI tractography is performed to evaluate the quality of the match. Although these studies constitute the natural first step in evaluating DTI tractography, they do not test DTI data in real physiological conditions.

The second approach relies on the in-vivo injection of manganese, an MRI visible enhancement contrast agent that can stain neural pathways. A comparison between the DTI image of principal direction (first eigenvalue) and the manganese stain distinguishable on the MRI image is proposed (Lin et al., 2001, 2003). While these studies are promising, to consider the Manganese as a gold standard would be premature since its specificity to trace neuronal connections is still being investigated (see Saleem et al., 2002 for an evaluation study using WGA-HRP as reference like in our study).

The third approach utilizes atlases based on histology or directly histological sections that are stained with a general cell marker such as cresyl violet; these slides, in turn, are compared to DTI images of principal direction (Xue et al., 1999; Stieltjes et al., 2001; Catani et al., 2002; Zhang et al., 2005). The histological approach is the most direct method of validation; however, this methodology cannot directly visualize axonal projections as can be done with neuronal tract tracers. Moreover, these studies were performed in 2D.

Thus, to improve upon the histological approach, we utilized a classical neuronal tract tracer injected directly into the brain of a macaque monkey. Labeled fibers, subsequently revealed on histological sections, were directly compared with corresponding tracts calculated from the in-vivo DTI data for the same animal. Our group presented preliminary qualitative results on postmortem DWI data of the fixed brain acquired following sacrifice in Peled et al. (2005); Dauguet et al. (2006).

Materials and methods

MR image acquisition

We performed in-vivo MR imaging of a macaque monkey brain on a 3 T General Electric MRI scanner; next, we conducted anatomical T1-weighted imaging using a standard 3D fast SPGR sequence with voxel dimensions $0.5 \times 0.5 \times 1$ mm^3. We performed DTI using a line scan diffusion imaging sequence (LSDI) sequence (Gudbjartsson et al., 1996) with one baseline T_2 (b-value=5 ms/mm^2) and 6 gradient directions with b-value of 750 ms/mm^2. The

acquired voxel dimensions were $1.5 \times 1.5 \times 1.5$ mm^3 zero-padded in-plane and interpolated between slices to $0.75 \times 0.75 \times 0.75$ mm^3. We utilized LSDI, as opposed to echo-planar imaging (EPI), because of its robustness in the face of magnetic susceptibility-induced artifacts.

Brain injection

Using procedures approved by the Harvard Medical Area Standing Committee on Animals, we performed craniotomies on the macaque under general anesthesia and pressure-injected 4% Wheat Germ Agglutinin conjugated to HRP (WGA-HRP) in sterile water under microscopic stereotaxic guidance.

Though we use the term in the discussion below, WGA is not a "stain" per se; it is rendered visible using a standard histochemical reaction. Five 0.2 μl injections were performed along both the pre- and post-central gyri. Three days later, we sacrificed the monkey; it was perfused with aldehyde fixative and the brain removed from the skull (see Berezovskii and Born, 2000 for more details concerning post-processing of the tissue).

Brain sectioning and histo-chemistry

We separated the brain into two blocks to facilitate sectioning and fixation. Next, we serially sectioned the entire brain in the coronal plane (80 μm thickness) using a freezing, sliding microtome. Prior to cutting each section, we photographed the block face using a rigidly mounted Hasselblad camera with a 25 megapixel Phase 1 digital back to facilitate subsequent 3D reconstruction.

Every eighth section was reacted for WGA-HRP using tetramethyl benzidine (Mesulam, 1978), producing a series of 90 sections spanning the entire brain. We then mounted these sections on glass slides and scanned them using both a GE Healthcare Amersham Typhoon 9410 in fluorescent transparency mode at 100 μm resolution and a regular flatbed scanner in reflection optical mode at 400 dpi resolution. Fluorescent scanning optimizes the gray/white matter contrast for registration purposes, whereas optical scanning allows differentiation of fiber staining for segmenting the bundles. A linear combination of these two scans produced a hybrid image with both good contrast and clear fiber staining. In this linear combination, the optical scanning images were inverted producing white areas of HRP-reacted tissue.

Photographic volume and spatial alignment

We first selected and stacked the block face photographs corresponding to the subset of stained and mounted histological slices; second, within each of the anterior and posterior blocks, directly stacked the block face photographs slice by slice; and third, assembled the anterior and posterior blocks together using an affine transformation estimated between the two sections facing at the intersection of the blocks. Within each block, the stack of photographs was directly 3D-consistent since we took each photograph repeatedly in the same position, section after section. Therefore, to render the whole block face volume 3D-consistent, we applied the affine transformation to stick the two blocks together. We refer to the resulting image data set as "the photographic volume".

We then co-aligned each histological slice on the corresponding photograph using per-hemisphere affine registration, which is accomplished by automatically segmenting the hemispheres and estimating an individual 2D affine transformation for each one

(Dauguet, 2005). The resulting volume of histological slices was geometrically similar to the 3D-consistent photographic volume; hence, we refer to this as "the histological volume".

We have estimated a 3D affine transformation followed by an elastic B-splines transformation (Free Form Deformation, FFD, Rueckert et al., 1999) between the photographic volume and the anatomical MRI data to compensate the mechanical and physiological deformations between the in-vivo and post-mortem brains (see Delzescaux et al., 2003). The cubic B-splines transformation was estimated by optimization of the mutual information criterion (Viola and Wells, 1997) using two pyramidal levels (level 1: grid of $6 \times 8 \times 4$ control points and downsampling of the images by 2 in each direction; level 2: grid of $12 \times 16 \times 8$ control points and full resolution). Finally, we applied these transformations to the histological volume to measure both MRI data and histological volume in the same geometry.

Tracing fiber bundles on histological volume and DTI data

We manually segmented the HRP-reacted regions within the histological volume by tracing them through the histological slices in both the original orientation as well as in the reformatted orthogonal views. Next, we segmented the histological volume before the elastic transformation to achieve better delineation and then resampled it in the MRI geometry.

For the DTI tractography, we segmented the injection sites visible on the histological volume (an accumulation of staining with high intensity) and then selected this region (defined for both pre- and post-central gyrus injections) as the seed region for the tractography performed in the DTI volume.

We utilized a standard hyperstreamline-based method for performing tractography (Westin et al., 2002) from the seed region. Specifically, we decided to study separately the influence of the fractional anisotropy (FA), radius of curvature (R) and discrete integration method step size (S) settings on the tractography performed. We performed all tractography tests with the 3DSlicer toolkit and viewer (readily available at http://www.slicer.org). While studying the influence of one parameter, the two others were set to their respective default values (FA=0.15, R=0.5 mm, S=0.5 mm). For each measurement, we converted the result of the DTI tractography into a binary image where voxels were colored from tracts and used for further comparison.

Using the Dice coefficient (a superimposition score between two regions, Dice, 1945), we evaluated the similarity between the segmentation derived from histology and the DTI tractographies performed with the different settings tested. More precisely, if we denote card(X) (for "cardinal") the number of elements (or voxels) in any region X, the Dice coefficient D between two regions A and B is defined as:

$$D(A, B) = \frac{2\text{card}(A \cap B)}{(\text{card}(A) + \text{card}(B))} \tag{1}$$

We have excluded the seed regions (always common to both histological and DTI segmentations) from the estimation of the Dice coefficient so as not to bias the measurement.

Furthermore, to better understand the distribution of the fibers derived from the DTI tractography outside of the histological segmentation, we computed the Dice coefficient with a tolerance on the superimposition of two voxels controlled by a distance parameter e. If the distance from a voxel of the histological seg-
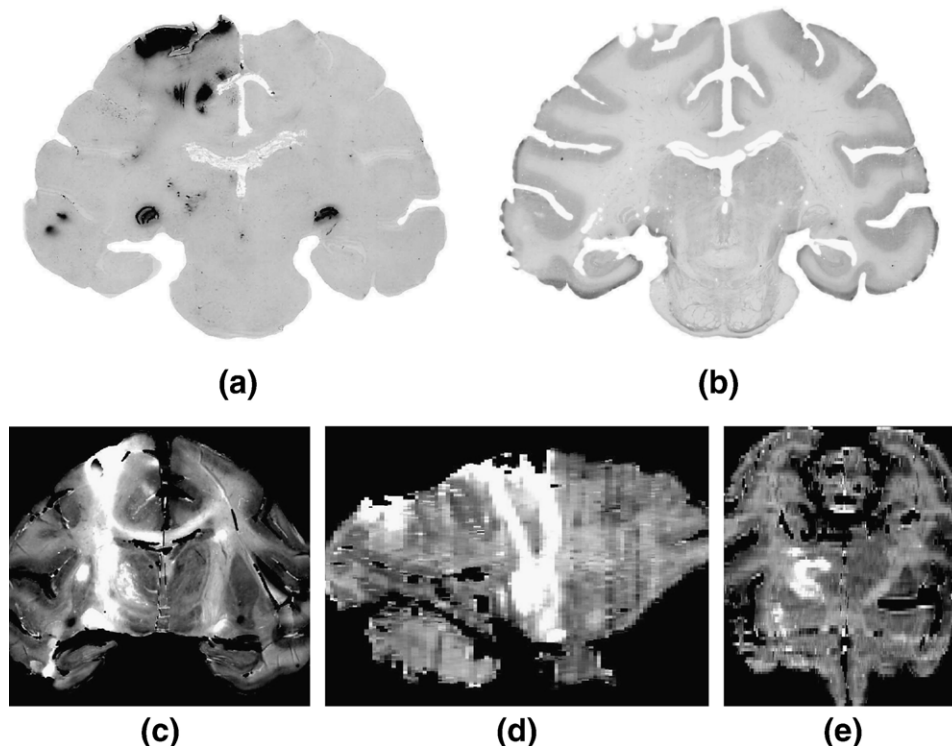

Fig. 1. Optical scan (a) and fluorescent scan (b) of a WGA-HRP stained section, which are combined to create a hybrid image. Reconstructed hybrid histological volume in coronal (c), sagittal (d) and axial (f) views. The tracts of interest are visible in bright white.

mentation (set A) to a DTI fiber (set B) is less than *e* (in mm), the voxel is counted in the DTI segmentation. This is equivalent to re-writing the Dice formula as follows:

$$D(A, B, e) = \frac{2\mathrm{card}(A \cap \mathrm{Dil}_A(B, e))}{(\mathrm{card}(A) + \mathrm{card}(\mathrm{Dil}_A(B, e)))} \qquad (2)$$

where $\mathrm{Dil}_A(B, e) = \{x \in \mathrm{Dil}(B, e) \,|\, x \in A\}$ stands for the special morphological dilation applied to *B* only if the added voxels belong to *A* (we noted $\mathrm{Dil}(B, e)$ the classical morphological dilation with radius *e* and a cubic structural element applied to *B*). The setting $e = 0$ corresponds to the classical Dice coefficient between *A* and *B*; for any *e* value, $D(A, B, e)$ ranges from 0 (no overlap) to 1 ($A = \mathrm{Dil}_A(B, e)$).

Results

The fiber bundles defined by histology

The WGA-HRP injections revealed the major connections in each area including (1) the descending axons from primary motor cortex through the internal capsule; (2) the ascending thalamocortical fibers to somatosensory cortex; and (3) the transcallosal pathways. The hybrid image, created as a linear combination of the fluorescent scanning and the color-inverted optical scanning, offered a good contrast for segmenting the staining using the coronal, sagittal and axial orientations (see Fig. 1). After re-sampling the 3D segmentation using the elastic transformation, we mapped the histological tracts onto the MRI data.

The DTI tractography

Since the WGA-HRP stain diffused around the injection site, the neighboring regions were similarly stained, and the injection sites were clearly visible on the histological volume in the pre- and post-central gyri. We mapped the segmented region onto the DTI data (Fig. 2) and used this as the seeding area for the tractography. The tractography algorithm relies mainly on the three parameters mentioned above, which characterize the behavior of the tract delineation. The fractional anisotropy (FA) threshold controls when the tractography may be stopped; the radius of curvature sets the tightest turn allowed; and the step size controls the spatial discretization for the integration method. The settings tested ranged from 0.00 to 0.60 with an increment of 0.05 for fractional anisotropy; from 0.0 mm to 1.0 mm with an increment of 0.1 for the radius of curvature; and finally, from 0.1 mm to 1.3 mm with an increment of 0.1 mm for the step size.

Comparison

For each of the three settings, we identified a single maximum peak value of Dice within the range of values tested for DTI tractography (Fig. 3). These maximums are reported in Table 1 for all the settings studied and for each of the four tolerance distances tested. The volumes of the tractography segmentations corresponding to the maximums were always greater than the volume of the histological segmentation, which demonstrates the tendency of DTI tractography to over segment on our data set the white matter pathways connections leading to a high proportion of false positives, as can be seen in Table 2 where all the volumes reported. We can see also in this volume table that the tractography
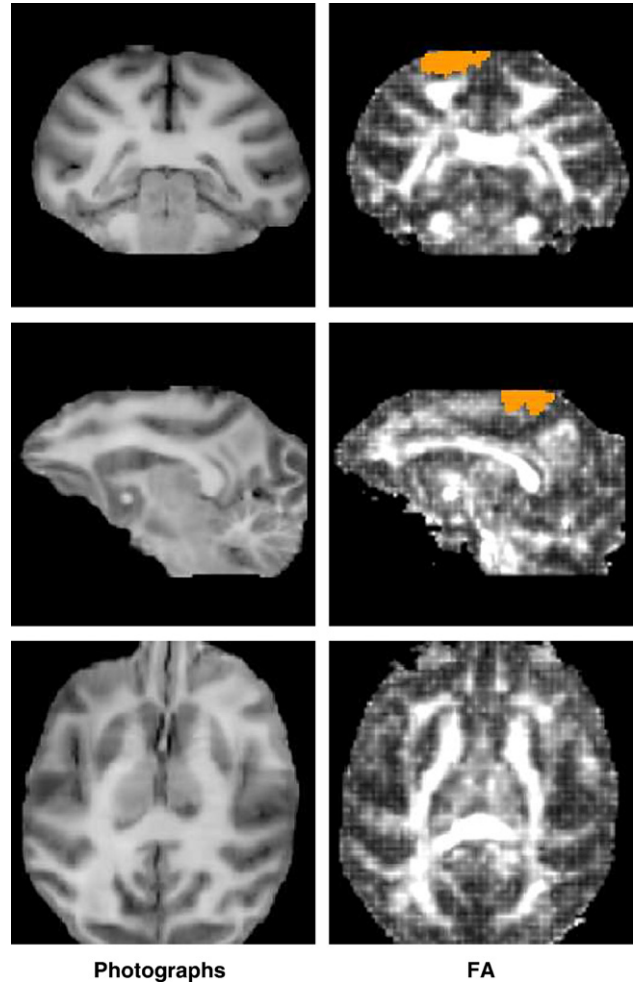

Fig. 2. Photographic volume in the in-vivo MRI geometry after 3D reconstruction and elastic correction (left) compared to fractional anisotropy (FA) image estimated from the DTI data (right). The segmented injection sites used as seed regions are shown in orange. From top to bottom: coronal, sagittal and axial views.

segmentation got less constrained as the anisotropy and radius of curvature settings increased, whereas it was the contrary for the step size parameter. As could be expected in the definition of the e-Dice coefficient $D(A, B, e)$ (Eq. (2)), the number of false positives did not depend on the distance parameter *e* since only true positives were added in the special dilation of the tractography segmentation. In Fig. 4, we show the results of the tractography corresponding to these optimal settings along with the histological segmentations. As mentioned before, we did not take the compact cluster of very small fibers around the injection site into account since we excluded the seed region from the Dice estimation to avoid bias.

The Dice coefficient plotted relative to the fractional anisotropy threshold in Fig. 3(a) stays stable until FA = 0.25 before a significant decline begins. The result of the DTI segmentation was clearly robust relative to the setting of the fractional anisotropy threshold within this range. Outside of this range, the fibers from the DTI segmentation were truncated and seemed less pertinent anatomically. The DTI tractography corresponding to the most optimal settings was in good visual agreement with the histological

(a) Influence of Anisotropy Threshold

(b) Influence of Radius of Curvature
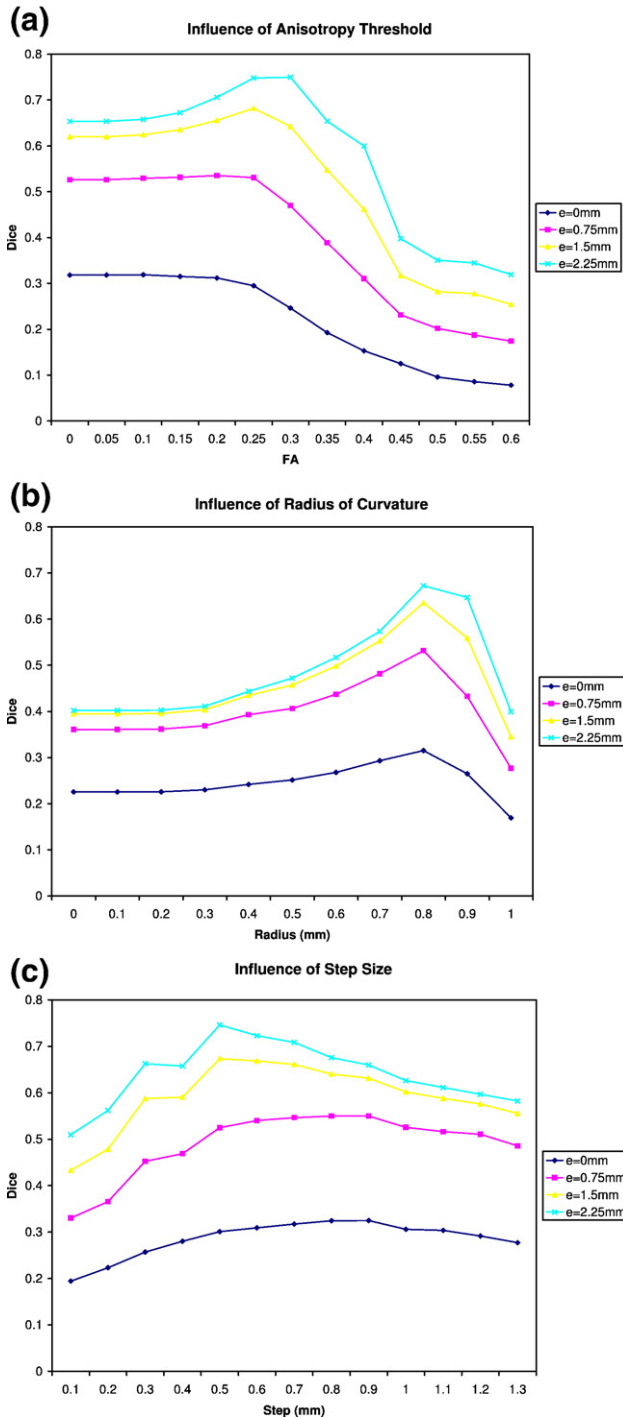
(c) Influence of Step Size

Fig. 3. Dice coefficient superimposition score between reference histological tract segmentation and segmentation derived from DTI tractography relatively to fractional anisotropy (FA) threshold (a), radius of curvature (R) threshold (b) and step size (c). The distance parameter e defines the distance in mm under which two pixels are considered superimposed.

segmentation, with few non-consistent branches outside of the segmentation. Yet, the tract did not extend far down from the injection seed region, and, with the exception of a single computed tracing, the tract stopped right under the corpus callosum when entering the thalamus where anisotropy drops down. The most

optimal setting found (FA=0.10) lies within the range of classical values used for DTI tractography.

For small values of the radius of curvature, the constraint on the curvature for some fibers was too low leading to non-realistic tracts—see Fig. 3(b). On the other hand, the Dice coefficient quickly dropped after the peak value because the constraint on the straightness of the tracts was too high. The tractography corresponding to the best match with histology was obtained for a classical radius of curvature threshold value. The tractography visually looked similar to the histological segmentation but seemed to go further, especially for the branch going through the corpus callosum, which continued to the cortex of the contra-lateral hemisphere with a tight turn. High values of radius of curvature seemed to facilitate tracing long fibers and going through regions of low anisotropy like relays or synapses.

The influence of step size, shown in Fig. 3(c), did not seem too high above the defaults value setting ($S \geq 0.5$ mm). The value corresponding to the best matching with histological segmentation ($S=0.9$ mm) was higher than expected, even though it is not strongly meaningful since the plot is relatively at in this range of values. The results of the DTI tractography for this setting were again globally in agreement with the histological segmentation, but they appeared somehow noisy with a few isolated and non-realistic fibers. The smoothness of the fibers was also reduced compared to the previous results.

The setting values of radius of curvature corresponding to the maximum Dice coefficient were the same for all the different values of the parameter e. This weak dependency suggests that the shape of the segmentation obtained for these settings matched the histological segmentation shape. As for the anisotropy and the step size optimal values, they were shifted forward (corresponding to more constrained tractographies) as the dilation parameter e increased, suggesting larger shape differences with the histological segmentation.

Discussion

The results globally show that the tracts derived from DTI correlate well visually with the corresponding pathways derived from direct tracing on histology, as shown in Fig. 4. In particular, the crossing between the pyramidal tract and the corpus callosum was handled correctly due to the high number of fibers traced from the seed region.

However, the best Dice scores obtained were surprisingly low. The segmentation of the staining on the histological volume can be a first source of error. The WGA-HRP reaction product accumulated in certain regions, and in others, did not saturate the

Table 1
Maximum Dice superimposition coefficients between histological and DTI fiber segmentation for different superimposition tolerance distances, e, while either the fractional anisotropy threshold, the radius of curvature or the step size is variable

Variable/e (mm)	$e=0$	$e=0.75$	$e=1.50$	$e=2.25$
Fractional anisotropy (FA)	0.32 (FA=0.10)	0.54 (FA=0.20)	0.68 (FA=0.25)	0.75 (FA=0.30)
Radius of curvature (R in mm)	0.32 (R=0.8)	0.53 (R=0.8)	0.64 (R=0.8)	0.67 (R=0.8)
Step size (S in mm)	0.32 (S=0.90)	0.55 (S=0.80)	0.67 (S=0.50)	0.75 (S=0.50)

Table 2
Volume of the tractography (DTI) segmentation compared to the histological injection staining (INJ.), volumes of false negative (FN) and false positive (FP) regions for the 3 sets of tractography parameters tested (FA, radius of curvature and step size) and for different e values

Variable	e (mm)	$e=0$				$e=0.75$				$e=1.5$				$e=2.25$			
	Volume (mm³)	DTI	INJ.	FN	FP	DTI	INJ.	FN	FP	DTI	INJ.	FN	FP	DTI	INJ.	FN	FP
FA	0	1622.53	1139.06	699.469	1182.94	2012.34	1139.06	309.656	1182.94	2225.81	1139.06	96.1875	1182.94	2309.77	1139.06	12.2344	1182.94
	0.05	1622.53	1139.06	699.469	1182.94	2012.34	1139.06	309.656	1182.94	2225.81	1139.06	96.1875	1182.94	2309.77	1139.06	12.2344	1182.94
	0.1	**1595.95**	**1139.06**	**702.844**	**1159.73**	1987.03	1139.06	311.766	1159.73	2202.61	1139.06	96.1875	1159.73	2286.56	1139.06	12.2344	1159.73
	0.15	1501.45	1139.06	723.094	1085.48	1890.84	1139.06	333.703	1085.48	2121.19	1139.06	103.359	1085.48	2212.31	1139.06	12.2344	1085.48
	0.2	1284.19	1139.06	761.062	906.188	**1653.75**	**1139.06**	**391.5**	**906.188**	1903.5	1139.06	141.75	906.188	2021.62	1139.06	23.625	906.188
	0.25	1000.69	1139.06	823.5	685.125	1344.09	1139.06	480.094	685.125	**1628.86**	**1139.06**	**195.328**	**685.125**	1774.83	1139.06	49.3594	685.125
	0.3	739.547	1139.06	907.875	508.359	1014.19	1139.06	633.234	508.359	1287.98	1139.06	359.438	508.359	**1496.39**	**1139.06**	**151.031**	**508.359**
	0.35	553.078	1139.06	976.219	390.234	759.375	1139.06	769.922	390.234	966.516	1139.06	562.781	390.234	1133.16	1139.06	396.141	390.234
	0.4	437.484	1139.06	1018.41	316.828	584.297	1139.06	871.594	316.828	753.891	1139.06	702	316.828	940.359	1139.06	515.531	316.828
	0.45	378.844	1139.06	1044.14	283.922	469.969	1139.06	953.016	283.922	552.234	1139.06	870.75	283.922	637.031	1139.06	785.953	283.922
	0.5	340.875	1139.06	1068.19	270	428.203	1139.06	980.859	270	501.609	1139.06	907.453	270	569.531	1139.06	839.531	270
	0.55	328.219	1139.06	1076.2	265.359	410.484	1139.06	993.938	265.359	491.484	1139.06	912.938	265.359	557.719	1139.06	846.703	265.359
	0.6	320.625	1139.06	1082.11	263.672	397.406	1139.06	1005.33	263.672	467.859	1139.06	934.875	263.672	530.297	1139.06	872.438	263.672
Radius (mm)	0	3950.86	1139.06	565.312	3377.11	4371.47	1139.06	144.703	3377.11	4487.06	1139.06	29.1094	3377.11	4512.8	1139.06	3.375	3377.11
	0.1	3950.86	1139.06	565.312	3377.11	4371.47	1139.06	144.703	3377.11	4487.06	1139.06	29.1094	3377.11	4512.8	1139.06	3.375	3377.11
	0.2	3936.94	1139.06	566.156	3364.03	4358.39	1139.06	144.703	3364.03	4473.98	1139.06	29.1094	3364.03	4499.72	1139.06	3.375	3364.03
	0.3	3821.34	1139.06	568.688	3250.97	4244.06	1139.06	145.969	3250.97	4360.92	1139.06	29.1094	3250.97	4386.66	1139.06	3.375	3250.97
	0.4	3397.78	1139.06	590.625	2849.34	3824.3	1139.06	164.109	2849.34	3956.77	1139.06	31.6406	2849.34	3985.03	1139.06	3.375	2849.34
	0.5	3058.17	1139.06	611.297	2530.41	3465.7	1139.06	203.766	2530.41	3617.58	1139.06	51.8906	2530.41	3664.83	1139.06	4.64062	2530.41
	0.6	2610.56	1139.06	637.031	2108.53	3016.83	1139.06	230.766	2108.53	3186	1139.06	61.5938	2108.53	3240.42	1139.06	7.17188	2108.53
	0.7	2160.42	1139.06	655.594	1676.95	2570.06	1139.06	245.953	1676.95	2752.31	1139.06	63.7031	1676.95	2808.84	1139.06	7.17188	1676.95
	0.8	**1501.45**	**1139.06**	**723.094**	**1085.48**	1890.84	1139.06	333.703	1085.48	2121.19	**1139.06**	103.359	1085.48	2212.31	1139.06	12.2344	1085.48
	0.9	811.266	1139.06	880.875	553.078	1020.09	1139.06	672.047	553.078	1209.52	1139.06	482.625	553.078	1362.23	1139.06	329.906	553.078
	1	550.547	1139.06	996.047	407.531	656.016	1139.06	890.578	407.531	729.844	1139.06	816.75	407.531	793.125	1139.06	753.469	407.531
Step (mm)	0.1	564.047	1139.06	973.688	398.672	702.844	1139.06	834.891	398.672	823.5	1139.06	714.234	398.672	924.75	1139.06	612.984	398.672
	0.2	680.062	1139.06	936.141	477.141	838.688	1139.06	777.516	477.141	985.5	1139.06	630.703	477.141	1108.69	1139.06	507.516	477.141
	0.3	775.406	1139.06	893.109	529.453	1017.14	1139.06	651.375	529.453	1223.44	1139.06	445.078	529.453	1355.91	1139.06	312.609	529.453
	0.4	875.391	1139.06	856.828	593.156	1123.45	1139.06	608.766	593.156	1318.78	1139.06	413.438	593.156	1441.55	1139.06	290.672	593.156
	0.5	1044.98	1139.06	810.422	716.344	1376.58	1139.06	478.828	716.344	**1658.39**	**1139.06**	**197.016**	**716.344**	**1820.39**	**1139.06**	**35.0156**	**716.344**
	0.6	1203.61	1139.06	777.094	841.641	1574.44	1139.06	406.266	841.641	1836.42	1139.06	144.281	841.641	1963.41	1139.06	17.2969	841.641
	0.7	1300.64	1139.06	752.203	913.781	1685.39	1139.06	367.453	913.781	1927.12	1139.06	125.719	913.781	2039.77	1139.06	13.0781	913.781
	0.8	1498.08	1139.06	711.281	1070.3	**1908.14**	**1139.06**	**301.219**	**1070.3**	2110.64	1139.06	98.7188	1070.3	2197.55	1139.06	11.8125	1070.3
	0.9	**1605.23**	**1139.06**	**693.562**	**1159.73**	2031.33	1139.06	267.469	1159.73	2219.91	1139.06	78.8906	1159.73	2291.62	1139.06	7.17188	1159.73
	1	1805.62	1139.06	688.5	1355.06	2243.95	1139.06	250.172	1355.06	2428.31	1139.06	65.8125	1355.06	2492.44	1139.06	1.6875	1355.06
	1.1	1904.77	1139.06	677.109	1442.81	2341.41	1139.06	240.469	1442.81	2517.75	1139.06	64.125	1442.81	2579.77	1139.06	2.10938	1442.81
	1.2	1984.92	1139.06	683.859	1529.72	2444.77	1139.06	224.016	1529.72	2608.45	1139.06	60.3281	1529.72	2664.56	1139.06	4.21875	1529.72
	1.3	2044.41	1139.06	697.781	1603.12	2482.73	1139.06	259.453	1603.12	2658.23	1139.06	83.9531	1603.12	2729.53	1139.06	12.6562	1603.12

The best settings for each e in terms of Dice scores (see Fig. 3 and Table 1) are indicated in bold.
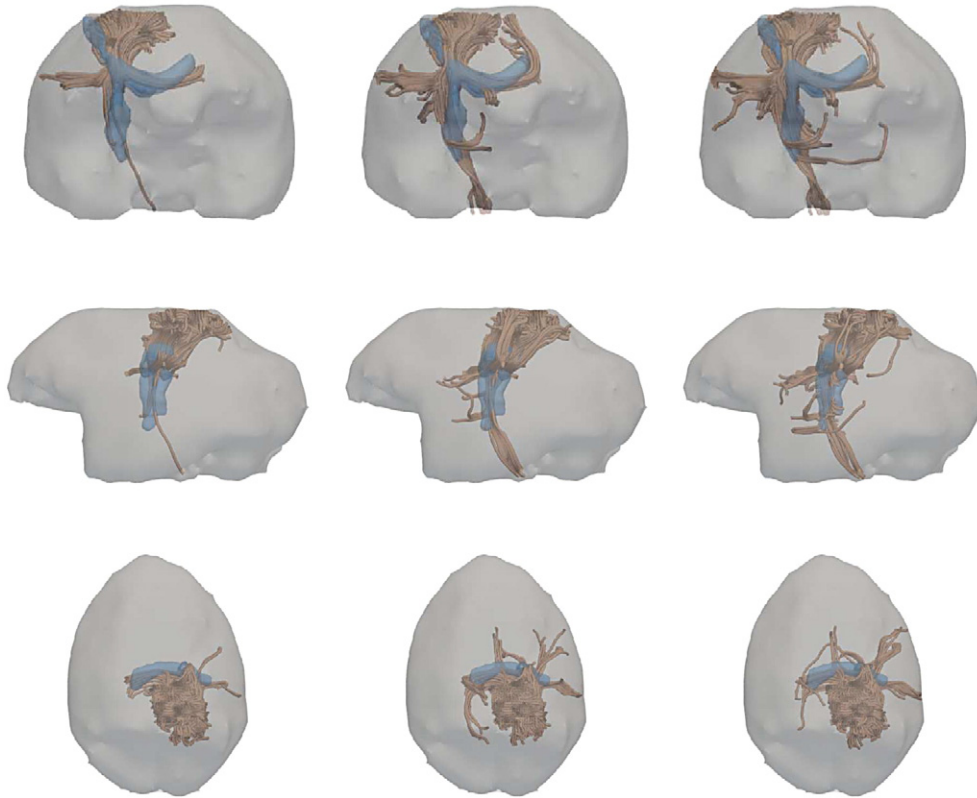
Fig. 4. Front, side and top views (from top to bottom) showing both the segmentation derived from histology (in blue) and the best results of the DTI tractography (fibers in brown) for the three settings tested: anisotropy influence, curvature influence and step size influence (from left to right) inside a surface rendering of the brain mask.

fibers until near their terminals, thus making accurate tracing more challenging. It is important to note that, although there was slight uncertainty on the precise location of the fibers stained, there was no ambiguity on the global shape of the tract as well as on the connectivity described by the starting and ending points.

Furthermore, the global in-vivo/post-mortem registration could have introduced some errors. The scheme utilized, as described in Dauguet (2005), has been shown to perform with less than 3% error on the global volume between the elastically corrected post-mortem geometry and the MRI data. At the scale of a tract, the remaining error could artificially make the superimposition score lower.

Using the HRP injection sites as seed regions appeared to be the most objective way to trace the same fibers as those stained on the histological sections. This strategy assumes that the saturation of axons and the DTI tractography follow the same behavior. Even if it is obviously globally the case, there appear to be minor dissimilarities. For instance, for most settings, the DTI tractography seeded from pre- and post-central cortex reaches the lowest level of the brain (pons); whereas, the staining stopped before (see Fig. 4). This may be due to the stain's inability to permeate a particular region, or because the further the stain is from the injection points, the less intense the stain. The horizontal branch of fibers from the DTI tractography going to the peripheral cortex also shows a divergence between both segmentations. This difference lowers the superimposition score significantly since it does not correspond to any branch of the histological segmentation. There is a possibility that this branch is anatomically pertinent even though it was not stained, or it may be an artifact of the tractography

algorithm. The recently widely used two-ROI approach based on anatomical a priori anatomical knowledge approach could also allow to perform more constrained tractography.

Therefore, the Dice coefficients estimated for $e = 0.75$ mm appear to be a reasonable choice to compensate for these errors. Furthermore, Dice coefficients above 0.50 indicate that the number of points in the intersection significantly increases when a tolerance of one voxel is allowed, proving that a considerable proportion of DTI fibers are not precisely inside, but less than a one voxel distance away from the histological segmentation. These results are more in agreement with what we expect visually. The remaining difference is still significant between the two segmentations, suggesting a cautious use of DTI tractography for fine measurements.

In summary, this study shows that DTI tractography identifies the main white matter pathways correctly. However, the results are dependent on the settings; and at the very fine fiber level, the confidence level of the anatomical accuracy of the segmentation is dramatically reduced. An example can be seen in Fig. 4: on the frontal view, for results corresponding to the step size influence (third column), fibers escaping from the main tract below the corpus callosum do not seem to be anatomically pertinent.

As settings appear to be a key factor for pertinent DTI tractography, a fine tuning of them is necessary to get reasonable results for each study. The graphs obtained for the influence of the settings suggest that the tuning of anisotropy threshold should not be too high (FA ≤ 0.15 for our data set). Furthermore, the tuning of the radius of curvature threshold should be in a defined range of values ($0.4 \geq R \geq 0.8$ for our data set), and the tuning of the step size

should not be too low ($S \geq 0.5$ for our data set). The low Dice scores obtained for small step values ($S < 0.5$) could be due to the difficulty of the tractography algorithm to pass through regions of low anisotropy (crossings, low end of fibers) when the progression step is too small, causing an early ending of the segmentation. This might be related to our specific data set, and to the fiber bundles tracked (mostly rectilinear). These results depend on the DTI acquisition parameters (resolution, number of directions, signal to noise ratio) which obviously play a crucial role for the relevance of the tractography performed, as well as the animal utilized in the study.

DTI tractography is an active research topic; new models aimed at improving the quality of the segmentation, especially in complex regions where fibers may cross, or in low anisotropy structures, are regularly proposed. Modeling of two or more tensors in each voxel, or using more complex distribution models for a diffusion coefficient, is an emerging research area that may help in solving these problems (Perrin et al., 2005; Bergmann et al., 2006; Peled et al., 2006).

Conclusion

In this paper, we have presented results visually and quantitatively comparing tracts derived from DTI tractography, and those derived from histological sections of a macaque brain. To enable direct comparisons, the data sets were spatially aligned to a common coordinate system using non-linear registration methods. To the best of our knowledge, this study is the first that compares long-range connectivity derived from histology in 3D and results from DTI tractography.

These results show, as expected, a general agreement between the tracts derived from histology and those derived from DTI tractography. However, we also note the influence of settings for the DTI tractography, which need to be fine-tuned; this is a necessary condition for pertinent fiber tracing. Moreover, substantial differences of location between the fibers were observed, either due to accumulated errors in the global protocol or to intrinsic imprecision of the tractography method tested, suggesting a cautious use of DTI tractography for fine measurements.

Future work will include studies on how to incorporate more complex diffusion models and tractography methods on different regions of the brain and in pathological cases. Indeed, understanding better DTI tractography, thanks to histology comparison, for patients with brain tumor or affected by neurodegenerative diseases is the cornerstone of its potential clinical applications.

Acknowledgments

References

Basser, P., Mattiello, J., LeBihan, D., 1994. Mr diffusion tensor spectroscopy and imaging. Biophys. J. 66, 259–267.

Basser, P., Pajevic, P., Pierpaoli, C., Duda, J., Aldroubi, A., 2000. In vivo fiber tractography using dt-mri data. Magn. Reson. Med. 44, 625–632.

Bentivoglio, M., Kuypers, H., Catsman-Berrevoets, C., Loewe, H., Dann, O., 1980. Two new uorescent retrograde neuronal tracers which are transported over long distances. Neurosci. Lett. 18 (1), 25–30.

Berezovskii, V., Born, R., 2000. Specificity of projections from wide-field and local motion-processing regions within the middle temporal visual area of the owl monkey. J. Neurosci. 20, 1157–1169.

Bergmann, Ø., Kindlmann, G., Lundervold, A., Westin, C.-F., 2006. Diffusion k-tensor estimation from q-ball imaging using discretized principal axesMICCAI'06. Lecture Notes in Computer Science. Springer Verlag, Copenhagen, Danemark.

Catani, M., Howard, R., Pajevic, S., Jones, D., 2002. Virtual in vivo interactive dissection of white matter fasciculi in the human brain. NeuroImage 17 (1), 77–94.

Dauguet, J., 2005. L'imagerie post mortem tridimensionnelle cérébrale: constitution et apport pour l'analyse conjointe de données histologiques anatomo-fonctionnelles et la mise en correspondance avec l'imagerie in vivo. PhD thesis, École Centrale de Paris.

Dauguet, J., Peled, S., Berezovskii, V., Delzescaux, T., Warfield, S., Born, R., Westin, C.-F., 2006. 3d histological reconstruction of fiber tracts and direct comparison with diffusion tensor mri tractography. Medical image computing and computer-assisted intervention (MICCAI 2006). LNCS. Springer Verlag, Copenhagen, Danemark, pp. 109–116.

Delzescaux, T., Dauguet, J., Condé, F., Maroy, R., Frouin, V., 2003. Using 3D non rigid d-based method to register post mortem 3D histological data and in vivo MRI of a baboon brain. In: Ellis, R.E., Peters, T.M. (Eds.), Medical Image Computing and Computer-Assisted Intervention (MICCAI 2003). LNCS, vol. 2879. Springer Verlag, Montreal, Canada, pp. 965–966.

Dice, L., 1945. Measures of the amount of ecologic association between species. Ecology 26, 207–302.

Glover, J., Petursdottir, G., Jansen, J., 1986. Fluorescent dextran-amines used as axonal tracers in the nervous system of the chicken embryo. J. Neurosci. Methods 18, 243–254.

Gudbjartsson, H., Maier, S.E., Mulkern, R.V., Mórocz, I.A., Patz, S., Jolesz, F.A., 1996. Line scan diffusion imaging. Magn. Reson. Med. 36, 509–519.

Hendry, I., Stockel, K., Thoenen, H., Iversen, L., 1974. The retrograde axonal transport of nerve growth factor. Brain Res. 68, 103–121.

Honig, M., Hume, R., 1986. Fluorescent carbocyanine dyes allow living neurons of identified origin to be studied in long-term cultures. J. Cell Biol. 103, 171–187.

Katz, L., Burkhalter, A., Dreyer, W., 1984. Fluorescent latex microspheres as a retrograde neuronal marker for in vivo and in vitro studies of visual cortex. Nature 310, 498–500.

Kuypers, H., Ugolini, G., 1990. Viruses as transneuronal tracers. Trends Neurosci. 13 (2), 71–75.

La Vail, J., La Vail, M., 1972. Retrograde axonal transport in the central nervous system. Science 176, 1416–1417.

LeBihan, D., Breton, E., Lallemand, D., 1986. MR imaging of intravoxel incoherent motions: application to diffusion and perfusion in neurologic disorders. Radiology 161, 401–407.

Lin, C., Tseng, W., Cheng, H., Chen, J., 2001. Validation of diffusion tensor magnetic resonance axonal fiber imaging with registered manganese-enhanced optic tracts. NeuroImage 14 (5), 1035–1047.

Lin, C., Weeden, V., Chen, J., Yao, C., Tseng, W., 2003. Validation of diffusion spectrum magnetic resonance imaging with manganese-enhanced rat optic tracts and ex vivo phantoms. NeuroImage 19 (3), 482–495.

Mesulam, M., 1978. Tetramethyl benzidine for horseradish peroxidase neurohistochemistry: a non-carcinogenic blue reaction product with

superior sensitivity for visualizing neural afferents and efferents. J. Histochem. 26.

Mori, S., Zhang, J., 2006. Principles of diffusion tensor imaging and its applications to basic neuroscience research. Neuron 51, 527–539.

Mori, S., Crain, B., Chacko, V., van Zijl, P., 1999. Three-dimensional tracking of axonal projections in the brain by magnetic resonance imaging. Ann. Neurol. 45.

Nolte, J., 2002. The Human Brain. An Introduction to Its Functional Anatomy, 5th edition. C.V. Mosby.

Peled, S., Berezovskii, V., Hendrickson, P., Born, R., Westin, C.-F., 2005. Histological validation of DTI using WGA-HRP in a macaque. Proc. ISMRM, Miami.

Peled, S., Friman, O., Jolesz, F., Westin, C.-F., 2006. Geometrically constrained two-tensor model for crossing tracts in dwi. Magn. Reson Imaging 24 (9), 1263–1270.

Perrin, M., Poupon, C., Rieul, B., Leroux, P., Constantinesco, A., Mangin, J.-F., Bihan, D.L., 2005. Validation of q-ball imaging with a diffusion bre-crossing phantom on a clinical scanner. Philos. Trans. R. Soc. B 360, 881–891.

Poupon, C., Clark, C.A., Frouin, V., Régis, J., Bloch, I., Bihan, D.L., Mangin, J.-F., 2000. Regularization of diffusion-based direction maps for the tracking of brain white matter fascicles. NeuroImage 12 (2), 184–195.

Rueckert, D., Sonoda, L.I., Hayes, C., Hill, D.L., Leach, M.O., Hawkes, D.J., 1999. Non-rigid registration using free-form deformations: application to breast mr images. IEEE Trans. Med. Imaging 18 (8), 712–721.

Saleem, K., Pauls, J., Augath, M., Trinath, T., Prause, B., Hashikawa, T., Logothetis, N., 2002. Magnetic resonance imaging of neuronal connections in the macaque monkey. Neuron 34 (5), 685–700.

Schwab, M., Javoy-Agid, F., Agid, Y., 1978. Labeled wheat germ agglutinin (wga) as a new, highly sensitive retrograde tracer in the rat brain hippocampal system. Brain Res. 152, 145–150.

Stieltjes, B., Kaufmann, W., van Zijl, P., Fredericksen, K., Pearlson, G., Solaiyappan, M., Mori, S., 2001. Diffusion tensor imaging and axonal tracking in the human brainstem. NeuroImage 14 (3), 723–735.

Stoeckel, K., Schwab, M., Thoenen, H., 1977. Role of gangliosides in the uptake and retrograde axonal transport of cholera and tetanus toxin as compared to nerve growth factor and wheat germ agglutinin. Brain Res. 132 (2), 273–285.

Tuch, D., 2004. Q-ball imaging. Magn. Reson. Med. 52, 1358–1372.

Viola, P., Wells, W.M., 1997. Alignment by maximization of mutual information. Int. J. Comput. Vis. 24, 137–154.

Westin, C.-F., Maier, S., Mamata, H., Nabavi, A., Jolesz, F., Kikinis, R., 2002. Processing and visualization of di usion tensor MRI. Med. Image Anal. 6, 93–108.

Xue, R., van Zijl, P., Crain, B., Solaiyappan, M., Mori, S., 1999. In vivo three-dimensional reconstruction of rat brain axonal projections by diffusion tensor imaging. Magn. Reson. Med. 42 (6), 1123–1127.

Zhang, J., Chen, Y.-B., Hardwick, J., Miller, M., Plachez, C., Richards, L., Yarowsky, P., Zijl, P., Mori, S., 2005. Magnetic resonance diffusion tensor microimaging reveals a role for bcl-x in brain development and homeostasis. J. Neurosci. 25 (8), 1881–1888.